DOI: 10.14529/jsfi250405

GPU-based Large-eddy Simulation of Mixed-phased Clouds

Evgeny V. Mortikov[1,2], ***Elizaveta M. Gashchuk***[1,2], ***Andrey V. Debolskiy***[1,2,3]

We discuss the development of the large-eddy simulation (LES) model of the atmospheric boundary layer with embedded two-moment bulk cloud microphysics scheme well-suited for massively-parallel heterogeneous supercomputers based on GPU (Graphics Processing Units) architecture. To evaluate the LES model and its computational efficiency, we consider the numerical setup corresponding to the development of an intense Arctic cold-air outbreak case. It is shown that the dynamic closure approach for calculation of subgrid scale fluxes, applied to both heat and moisture transport, allows to correctly reproduce moist convective boundary layers with mixed-phased clouds even with coarse grid resolution. Implementation of state-of-the-art microphysics scheme for GPU systems not only led to significant speedup of the computations, but in general improved the multi-GPU scaling of the model.

Keywords: large-eddy simulation, boundary layer turbulence, cloud-resolving modeling, computational performance, graphics processing unit.

Introduction

The atmospheric processes are characterized by a large spectra of motions. With a ratio of largest-to-smallest scales approaching ten orders of magnitude [46] they range from planetary waves (10^8 m) and cyclones to convective and cloud processes and finally to microscale turbulence (10^{-2} m). The rise in supercomputer performance in general coincides with grid refinement in state-of-the-art large-scale numerical weather prediction (NWP) and climate models, allowing to resolve increasingly larger span of scales and, in turn, to improve model predictions.

While cloud-resolving simulations are still (and will be in coming decades) a complex computational challenge for global atmospheric models [39], where convective processes are parameterized using RANS (Reynolds-Averaged Navier–Stokes) closures [34], the large-eddy simulation approach allows to explicitly reproduce the largest and most energy-containing scales contributing to both turbulence mixing and cloudy convection owing to the self-similarity of turbulence in the inertial range. This allows to study inherently linked turbulence, cloud-scale circulations and microphysical processes.

Unfortunately, the LES approach with available HPC resources in most cases is limited to diurnal studies and spatial scales reaching at best the order of 10 km. Current developments, see review [40], in numerical models and their optimization for supercomputers seem to bring the gap closer between NWP (at least for regional scale models) and LES. However, there is still a long way ahead, with the largest uncertainties related to representation of land surface-atmosphere interaction processes and the lack of turbulence closures suited for the so-called "grey-zone" resolution, where both LES and RANS underlying assumptions may fail.

One of our overall goals is the development of LES models, which are able to reproduce the atmospheric boundary layer (ABL) turbulence even with coarse resolution approaching "grey-zone" restrictions, while allowing to study the interaction of microscale processes and mesoscale organization of cloud clusters [42] with feasible simulations in domains of the order of

[1]Research Computing Center, Lomonosov Moscow State University, Moscow, Russia
[2]Moscow Center of Fundamental and Applied Mathematics, Moscow, Russia
[3]A. M. Obukhov Institute of Atmospheric Physics, Moscow, Russia

10–100 km. The former sets stringent requirements for the subgrid/subfilter closure, while the evident prerequisite for the latter is an efficient implementation of the model on supercomputers. GPU-accelerated HPC systems may provide a significant increase in computational performance of numerical models, e.g., see [3], where 150× speedup compared to CPU (Central Processing Unit)-only code was achieved in large-eddy simulation of pollutant dispersion and [40], where a LES model supplemented with single-moment ice microphysics scheme was implemented using CUDA.

In this paper we discuss the implementation of a large-eddy simulation model of the ABL with embedded bulk two-moment microphysics scheme capable of reproducing complex mixed-phase cloud processes on GPU-based architecture. We assess both the efficiency of GPU implementation and the sensitivity of the LES model to grid resolution in reproducing an intense Arctic cold-air outbreak case. Bulk microphysics schemes have some notable problems due to simplification in representing collection and sedimentation processes, compared with much computationally demanding bin-based or spectral models [26]. Despite this, they are commonly used in both cloud-resolving LES and large-scale NWP and climate models. In particular, we consider the two-moment cloud microphysics scheme [41, 43], which with some modifications is used in DALES [21] and PALM [29] atmospheric boundary layer LES codes, COSMO [1] and ICON [16] NWP models. In this regard, the results obtained in this study may be useful for improving such models as well.

The paper is structured as follows. In Section 1 we give an overview of the LES governing equations and the subgrid turbulence closure. The cloud microphysics scheme for liquid-phase and mixed-phases processes is presented in Section 2. The numerical aspects of the model and its implementation for supercomputers are given in Section 3. In Section 4 we assess the LES model and its efficiency on GPU architecture, followed by summary and conclusions.

1. Governing Equations and Subgrid-scale Model

We consider the dynamics of a stratified atmosphere governed by the Navier–Stokes equations in the Boussinesq approximation, which is described by a coupled system comprising momentum, continuity, heat and moisture transport equations:

$$\frac{\partial \overline{u}_i}{\partial t} + \frac{\partial \overline{u}_i \overline{u}_j}{\partial x_j} = -\frac{\partial \tau_{ij}}{\partial x_j} - \frac{1}{\rho_0}\frac{\partial \overline{p}}{\partial x_i} + \nu \frac{\partial^2 \overline{u}_i}{\partial x_j \partial x_j} + \varepsilon_{ij3} f \overline{u}_j + \overline{F}_i, \tag{1}$$

$$\frac{\partial \overline{u}_i}{\partial x_i} = 0, \tag{2}$$

$$\frac{\partial \overline{\Theta}}{\partial t} + \frac{\partial \overline{u}_i \overline{\Theta}}{\partial x_i} = -\frac{\partial h_{\Theta,i}}{\partial x_i} + \chi_\Theta \frac{\partial^2 \overline{\Theta}}{\partial x_i \partial x_i} + \overline{\Phi}_\Theta + \overline{F}_\Theta, \tag{3}$$

$$\frac{\partial \overline{q}}{\partial t} + \frac{\partial \overline{u}_i \overline{q}}{\partial x_i} = -\frac{\partial h_{q,i}}{\partial x_i} + \chi_q \frac{\partial^2 \overline{q}}{\partial x_i \partial x_i} + + \overline{\Phi}_q + \overline{F}_q, \tag{4}$$

where $\overline{\mathbf{u}} = (\overline{u}_1, \overline{u}_2, \overline{u}_3) \equiv (\overline{u}, \overline{v}, \overline{w})$ denotes the wind velocity vector with components aligned along the coordinates $\mathbf{x} = (x_1, x_2, x_3) \equiv (x, y, z)$, respectively, $\overline{p}$ is the pressure and ρ_0 is the reference air density, ν and $\chi_{[\Theta,q]}$ stand for coefficients of molecular kinematic viscosity and diffusivity, t is time. The term $\varepsilon_{ij3} f \overline{u}_j$ accounts for the Coriolis acceleration, where ε_{ijk} is the Levi-Civita symbol (alternating tensor), $f = 2\Omega \sin\phi$ – Coriolis parameter for latitude ϕ and Ω is the angular speed of Earth's rotation. The vector $\overline{F}_i$ corresponds to external forces acting on the flow, $\overline{\Phi}_{[\Theta,q]}$ are tendencies due to cloud microphysical processes and $\overline{F}_{[\Theta,q]}$ are any other

sinks or sources of heat and moisture. For stratified atmosphere $\overline{F}_i$ includes the buoyancy force $\overline{\mathbf{F}}_b = \alpha g \overline{\Theta}_v \cdot \mathbf{e}_3$, where

$$\overline{\Theta}_v = \overline{\Theta}_p \left[1 + \left(\frac{R_v}{R_d} - 1 \right) \overline{q}_v - \overline{q}_{\text{liquid}} - \overline{q}_{\text{solid}} \right] \tag{5}$$

is the virtual potential temperature equivalent to potential temperature $\overline{\Theta}_p$ in dry air, $\overline{q}_{[v,\text{liquid,solid}]}$ are the water vapor, liquid water and solid water mixing ratios, respectively, $R_{[d,v]}$ are the specific gas constants for dry air and water vapor, α is the thermal expansion coefficient, g is the acceleration due to gravity and $\mathbf{e}_3$ is the unity vector in the vertical z direction (positive upwards). We consider prognostic equations (3), (4) for conservative (in terms of wet adiabatic processes, e.g., condensation/evaporation) variables – the total water content $\overline{q} = \overline{q}_v + \overline{q}_{\text{liquid}} + \overline{q}_{\text{solid}}$ and the liquid/solid water potential temperature $\overline{\Theta}$:

$$\overline{\Theta} = \overline{\Theta}_p - \frac{L_v}{c_p \Pi} \overline{q}_{\text{liquid}} - \frac{L_s}{c_p \Pi} \overline{q}_{\text{solid}}, \tag{6}$$

where $\Pi = (p_h/p_0)^{R_d/c_p}$ is the Exner function with hydrostatic pressure p_h non-dimensionalized by reference value p_0, c_p is the heat capacity of dry air at constant pressure, $L_{[v,s]}$ are constants attributed to latent heat of vaporization and sublimation, respectively. The liquid $\overline{q}_{\text{liquid}}$ and "solid" (i.e., ice) $\overline{q}_{\text{solid}}$ water content mixing ratios are calculated by the cloud microphysics part of the model, which is described in subsequent section.

The $\overline{(\cdot)}$ in the system of equations (1)–(4) denotes spatial filtering applied in the LES approach, $\overline{a}(\mathbf{x}, t) = F_{\overline{\Delta}} a(\mathbf{x}, t)$, where $\overline{\Delta}$ is the filter width and a is any scalar variable or vector component. The subfilter or subgrid-scale (as the filter width is related to the grid spacing of the discrete system) stress terms τ_{ij} and scalar fluxes $h_{a,i}$ are expressed as:

$$\tau_{ij} = \overline{u_i u_j} - \overline{u}_i \overline{u}_j, \tag{7}$$

$$h_{a,i} = \overline{u_i a} - \overline{u}_i \overline{a}, \tag{8}$$

where, e.g., $a = [\Theta, q]$. The system of equations (1)–(4) requires turbulence closure and the subfilter terms have to be defined in terms of resolved (filtered) variables.

We use the well-known dynamic Smagorisnky eddy viscosity model [38], which implies that the anisotorpoic part τ^a_{ij} of τ_{ij} tensor is aligned with the strain rate of the resolved scales:

$$\tau^a_{ij} = \tau_{ij} - \frac{1}{3} \delta_{ij} \tau_{kk} \approx \tau^{\text{smag}}_{ij} = -2 K_m \overline{S}_{ij}, \tag{9}$$

where $\overline{S}_{ij}$ denotes the strain rate tensor of the filtered velocity field:

$$\overline{S}_{ij} = \frac{1}{2} \left(\frac{\partial \overline{u}_i}{\partial x_j} + \frac{\partial \overline{u}_j}{\partial x_i} \right). \tag{10}$$

Here the eddy viscosity coefficient K_m is defined as:

$$K_m = \left(C_s \overline{\Delta} \right)^2 \left| \overline{S} \right|, \tag{11}$$

where C_s is the Smagorinsky coefficient and $\left| \overline{S} \right| = \sqrt{2 \overline{S_{ij} S_{ij}}}$ is the tensor norm.

The subgrid/subfilter-scale fluxes of temperature Θ and total water content q are expressed in the same vein using the eddy diffusivity hypothesis:

$$h_{\Theta,i} = -K_{\Theta,h}\frac{\partial\overline{\Theta}}{\partial x_i} = -K_m Pr_{\rm sgs}^{-1}\frac{\partial\overline{\Theta}}{\partial x_i}, \tag{12}$$

$$h_{q,i} = -K_{q,h}\frac{\partial\overline{q}}{\partial x_i} = -K_m Sc_{\rm sgs}^{-1}\frac{\partial\overline{q}}{\partial x_i}, \tag{13}$$

where $Pr_{\rm sgs}$ and $Sc_{\rm sgs}$ are the subgrid Prandtl and Schmidt numbers, respectively, which we assume may be distinct for heat and moisture fluxes.

The dynamic procedure [27] based on the Germano identity [15] is applied for calculation of the Smagorinsky coefficient, $C_s \equiv C_s(\mathbf{x},t)$, and $Pr_{\rm sgs}(\mathbf{x},t)$, $Sc_{\rm sgs}(\mathbf{x},t)$ dependent on spatial coordinates and time. The Lagrangian averaging along the flow pathlines, as proposed in [5, 30], is used for solving the resulting minimization problem. Assuming that exponentially decaying weights are used in the averaging, the problem reduces to simple relaxation-transport equations, which may be efficiently solved with first-order approximation in time, see [50] for details. The dynamic procedure defines subgrid Prandtl $Pr_{\rm sgs}(\mathbf{x},t)$ and Schmidt numbers $Sc_{\rm sgs}(\mathbf{x},t)$ without additional *ad hoc* assumptions on the flow dynamics, and is known to improve the model performance in simulations of stably stratified atmospheric boundary layers on coarse grids [9, 25].

2. Cloud Microphysics

The cloud microphysics model is based on the two-moment bulk scheme, proposed in [41, 43]. In the liquid-phase only case it assumes separation of droplet spectrum by radii threshold r_{th} in two parts, corresponding to cloud droplets $r < r_{th}$ and rain droplets $r \geq r_{th}$. In the two-moment approach only the first two moments of each part of spectra are predicted. The system of equations (1)–(4) is supplemented with prognostic equations for number concentrations of cloud and rain droplets, $\overline{N}_c$ and $\overline{N}_r$, and mixing ratios of cloud and rain water content, $\overline{q}_c$ and $\overline{q}_r$:

$$\frac{\partial\overline{N}_a}{\partial t} + \frac{\partial\overline{u}_i\overline{N}_a}{\partial x_i} = -\frac{\partial h_{N_a,i}}{\partial x_i} + \chi_{N_a}\frac{\partial^2\overline{N}_a}{\partial x_i\partial x_i} + \overline{\Phi}_{N_a}, \tag{14}$$

$$\frac{\partial\overline{q}_a}{\partial t} + \frac{\partial\overline{u}_i\overline{q}_a}{\partial x_i} = -\frac{\partial h_{q_a,i}}{\partial x_i} + \chi_{q_a}\frac{\partial^2\overline{q}_a}{\partial x_i\partial x_i} + \overline{\Phi}_{q_a}, \tag{15}$$

where $a = [c, r]$ and $\overline{q}_{\rm liquid} = \overline{q}_c + \overline{q}_r$. The terms Φ in the right-hand side stand for different cloud microphysics processes. For liquid part of cloud model these are:

$$\overline{\Phi}_{N_c} = \left.\frac{\partial\overline{N}_c}{\partial t}\right|_{\rm act} + \left.\frac{\partial\overline{N}_c}{\partial t}\right|_{\rm evap} + \left.\frac{\partial\overline{N}_c}{\partial t}\right|_{\rm auto} + \left.\frac{\partial\overline{N}_c}{\partial t}\right|_{\rm accr} + \left.\frac{\partial\overline{N}_c}{\partial t}\right|_{\rm sed}, \tag{16}$$

$$\overline{\Phi}_{N_r} = \left.\frac{\partial\overline{N}_r}{\partial t}\right|_{\rm auto} + \left.\frac{\partial\overline{N}_r}{\partial t}\right|_{\rm slf/brk} + \left.\frac{\partial\overline{N}_r}{\partial t}\right|_{\rm evap} + \left.\frac{\partial\overline{N}_r}{\partial t}\right|_{\rm sed}, \tag{17}$$

$$\overline{\Phi}_{q_c} = \left.\frac{\partial\overline{q}_c}{\partial t}\right|_{\rm cond} + \left.\frac{\partial\overline{q}_c}{\partial t}\right|_{\rm evap} + \left.\frac{\partial\overline{q}_c}{\partial t}\right|_{\rm auto} + \left.\frac{\partial\overline{q}_c}{\partial t}\right|_{\rm accr} + \left.\frac{\partial\overline{q}_c}{\partial t}\right|_{\rm sed}, \tag{18}$$

$$\overline{\Phi}_{q_r} = \left.\frac{\partial\overline{q}_r}{\partial t}\right|_{\rm auto} + \left.\frac{\partial\overline{q}_r}{\partial t}\right|_{\rm accr} + \left.\frac{\partial\overline{q}_r}{\partial t}\right|_{\rm evap} + \left.\frac{\partial\overline{q}_r}{\partial t}\right|_{\rm sed}. \tag{19}$$

The tendencies correspond to activation of cloud droplets (act), represented by Twomey-type parameterizations linking cloud condensation nuclei with prescribed dry aerosol number concentration, condensation (cond) and evaporation (evap) of cloud and rain droplets, autoconversion (auto) of cloud droplets to rain, accretion (accr), merging and splitting of rain droplets (slf/brk), with the latter affecting only the number concentration $\overline{N}_r$. Their formulation is given in [41, 43, 44] and assumes that droplet spectra follows a gamma distribution and that the distribution's slope and shape parameters may be estimated based on predicted bulk characteristics. The sedimentation tendencies (sed) are calculated using a simple upwind scheme.

We use the extension of the two-moment scheme for mixed-phase clouds as described in [41], where additional prognostic equations are considered for both number concentrations and mixing ratios of three hydrometeors: cloud ice, snow and graupel, e.g., $a = [i, s, g]$ in (14) and (15), $\overline{q}_{\text{solid}} = \overline{q}_i + \overline{q}_s + \overline{q}_g$. The microphysics scheme assumes power-law relations for diameter-mass and velocity-mass relations for each category, as well as generalized gamma particle size distributions.

The mixed-phase scheme accounts for primary ice production processes – ice nucleation following [37], homogeneous/heterogeneous freezing [4, 7] of cloud and rain droplets, and considers ice multiplication parameterization by the Hallett-Mossop processes, which occurs due to riming of ice particles. The tendencies in equations for number concentrations and mixing ratios of ice, snow and graupel hydrometeors also include deposition (with ventilation coefficients for spherical particles), riming, aggregation and self-collection of snow, partial conversion of snow and ice crystals to graupel, collection of snow by graupel, sublimation, evaporation, melting and its enhancement due to collisions with liquid droplets in temperature range above freezing. The collection processes between different categories are formulated using a generalized approach suggested by [55], where the use of gamma-distribution for particle size and mass-diameter power-law relations allows to evaluate collection integrals analytically in terms of Gamma-functions in a unified manner.

The sedimentation tendencies of all hydrometeors are non-conservative and included in equations for liquid/solid water potential temperature $\overline{\Theta}$ and total water content $\overline{q}$:

$$\overline{\Phi}_\Theta = -\frac{L_v}{c_p \Pi}\left(\left.\frac{\partial \overline{q}_c}{\partial t}\right|_{\text{sed}} + \left.\frac{\partial \overline{q}_r}{\partial t}\right|_{\text{sed}}\right) - \frac{L_s}{c_p \Pi}\left(\left.\frac{\partial \overline{q}_i}{\partial t}\right|_{\text{sed}} + \left.\frac{\partial \overline{q}_s}{\partial t}\right|_{\text{sed}} + \left.\frac{\partial \overline{q}_g}{\partial t}\right|_{\text{sed}}\right), \tag{20}$$

$$\overline{\Phi}_q = \left.\frac{\partial \overline{q}_c}{\partial t}\right|_{\text{sed}} + \left.\frac{\partial \overline{q}_r}{\partial t}\right|_{\text{sed}} + \left.\frac{\partial \overline{q}_i}{\partial t}\right|_{\text{sed}} + \left.\frac{\partial \overline{q}_s}{\partial t}\right|_{\text{sed}} + \left.\frac{\partial \overline{q}_g}{\partial t}\right|_{\text{sed}}. \tag{21}$$

The time-advancement of the cloud microphysics model supports both the sequential-tendency splitting and parallel splitting approaches [11]. In the former during a single time step all tendencies associated with different processes (e.g., for the liquid-phase part of the model these are the terms appearing in the right-hand side in (16)–(19)) are calculated sequentially taking into account the tendencies evaluated beforehand. In the latter case, which will be used in GPU performance analysis in the subsequent section, all tendencies are calculated using the same state variables as they are given at the beginning of the time step. The subgrid terms $h_{N_a,i}$ and $h_{q_a,i}$ in (14) and (15) are evaluated using the eddy diffusivity of total water content $K_{q,h}$, i.e., the dynamic procedure is applied to conservative scalars $\overline{\Theta}$ and $\overline{q}$ only.

The cloud model supports some further simplifications. In particular, assuming that $\overline{N}_{[c,i]}$ represent fixed quantities or distributions and, moreover, that any supersaturation is removed in cloud or ice water content instantaneously. In this case, $\overline{q}_c$ and $\overline{q}_i$ are diagnostic parameters evaluated using the saturation adjustment procedure by considering excess water content $\overline{q}_v - \overline{q}_{sat}$ ($\overline{q}_v > \overline{q}_{sat}$) above saturation mixing ratio $\overline{q}_{sat}$ over water and ice surfaces. This partition of

excessive vapor between cloud droplets and ice crystals depends on absolute temperature of air $\overline{T} \equiv \overline{\Theta}_p \Pi$, see [51] for details.

The implementation of the two-moment bulk microphysics scheme was verified using extensive datasets of LES intercomparison studies, in particular, simulations of trade wind cumulus convection [45], precipitating cumulus-topped boundary layers [52] and mixed-phase stratiform Arctic clouds [36].

3. Numerical Implementation

The large-eddy simulation model with embedded two-moment mixed-phase microphysics bulk scheme was implemented as part of the DNS-, LES- and RANS- unified C/C++ code developed at the Lomonosov Moscow State University and the Marchuk Institute of Numerical Mathematics of the Russian Academy of Science [32, 33, 35]. The unified code is designed for numerical modeling of geophysical turbulent flows, includes an extensive set of LES and RANS subgrid closures [17, 18, 50], and was used in studies of the atmospheric boundary layer [9, 20, 25, 47, 48] and for large-eddy and direct numerical simulation (DNS) of urban canopy [18, 49, 53] and channel flows [2, 24].

The code makes use of hybrid MPI/OpenMP/CUDA approach for CPU and GPU computations, however, any possible optimizations due to OpenMP are omitted from this study. The MPI CPU-only implementation was used in large scale simulations of turbulent flows with the grid size of the order of 10^8 cells, e.g., see [57, 58]. The code supports 1D, 2D or 3D spatial decomposition of the computational grid among MPI-processes with common optimizations for improving scaling on HPC systems. This, in particular, includes options for combining MPI data transfers for a number of arrays (e.g., vector or tensor components) or increasing the width of the grid halo region [10] for reducing MPI communications latency. The latter allows to lower the number of calls to MPI functions but at the cost of additional computational overhead, which may be negligible when the size of the problem on MPI-process is comparatively small. The bulk cloud microphysics model was implemented supporting both CPU and GPU computations with additional optimizations for tracer transport equations proposed in [12, 33] for HPC systems.

The numerical method is based on conservative in momentum and energy second-order finite-difference approximation [31] of governing equations (1)–(4) on rectangular grids with staggered arrangement of nodes. The projection method [6] is applied for the time advancement of momentum equations (1) coupled with incompressibility constraint (2). Explicit third-order Adams–Bashforth scheme is used for the approximation in time of scalar transport equations (3), (4), (14), (15) and for the calculation of non divergence-free intermediate velocity at the first step of the projection method.

Biconjugate gradient stabilized (BiCGstab) iterative method with a V-cycle geometric multigrid preconditioner is used for solving the finite-difference approximation of the Poisson equation. On each grid in the multigrid sequence smoothing iterations are performed by successive upper relaxation method (SOR) for red-black ordering of nodes. The projection onto coarse grid and the prolongation operator onto a fine grid correspond to a bilinear interpolation consistent with the averaging operator used in finite-difference stencils.

In the LES subgrid closures we define the filter width $\overline{\Delta}$ as equal to the geometric mean of grid cell widths, $\overline{\Delta} = (\Delta_x \Delta_y \Delta_z)^{1/3}$. The dynamic procedure requires explicit definition of test filter $F_{\widehat{\Delta}}$, which is chosen the same as the ones used in [19, 50], while the filter width ratio α is calculated according to [28]. The filtering operations incur considerable additional MPI

communications and the filters are applied for each dimension of the 3D field sequentially to reduce the number of computations. Due to high computational cost (see analysis in [50, 54]) the dynamic procedure for the evaluation of Smagorinsky constant $C_s(\mathbf{x}, t)$, the subgrid Prandtl $Pr_{\text{sgs}}(\mathbf{x}, t)$ and Schmidt numbers $Sc_{\text{sgs}}(\mathbf{x}, t)$ is applied only every three integration time steps.

4. LES Model Evaluation

4.1. Cold-air Outbreak Case

We consider the numerical setup proposed in the COMBLE (Cold-Air Outbreaks in the Marine Boundary Layer Experiment) model-observation intercomparison project [13, 14, 23, 56], which aims to foster studies of key cloud microphysics and aerosol processes interactions and, in particular, evaluate LES and single-column models (SCM) capabilities in reproducing an intense supercooled cold-air outbreak (CAO) case observed over the Norwegian sea on 13 March 2020. Here the transition from ice surface to open water results in formation of a growing convective boundary layer (CBL) with mixed-phase clouds and stratocumulus to cumulus transition.

The setup emulates transition of air mass in Lagrangian frame of reference (over ~ 1000 km distance) with development of Arctic convective cloud features under strong CAO conditions with spatially variable forcing converted to time-varying surface temperature and time- and height-varying geostrophic wind for a horizontally homogeneous domain. Periodic boundary conditions are set in horizontal directions: $\phi(x = L_x, t) \equiv \phi(x = 0, t)$ and $\phi(y = L_y, t) \equiv \phi(y = 0, t)$, where ϕ is any scalar variable or vector component. The surface layer momentum, sensible and latent heat fluxes are calculated using MOST (Monin–Obukhov Similarity Theory) approximation in each surface grid cell using Businger–Dyer stability functions [9]. The momentum and thermal roughness values are kept fixed, with values close to the ones obtained in simulations with dynamic water surface roughness using Charnock parameterization (see analysis of sensitivity to roughness parameterizations in [23]).

The size of the domain is $L_x \times L_y \times L_z \equiv 25{\times}25{\times}7$ km^3. At the top of the domain free-slip and zero flux boundary conditions are applied to horizontal components of momentum and scalars, respectively. We follow the COMBLE part I configuration, which fixes cloud droplet number concentration and for mixed-phase simulations prescribes diagnostic ice formation with homogeneous freezing of drops also included.

The LES and SCM intercomparison results are available in [23] and on the project website [22] (and include the MSU/INM LES model). In this paper we focus on evaluation of LES subgrid model and the efficiency of GPU-computations. Note that we do not consider any long-wave radiation heating to remove any influence of external packages and libraries (i.e., MSU/INM LES model uses the RRTMG library for long-wave radiation transfer in cloudy atmosphere [8], which depending on temporal and vertical discretization of the radiation scheme may take up to 90% of computational time) on the performance of the LES model with embedded cloud microphysics scheme.

4.2. Grid Resolution Sensitivity

The COMBLE case represents a suitable scenario to assess model performance and sensitivity to grid resolution and subgrid closure, as it includes strong turbulence convection and

precipitation events with complex mixed-phase cloud interactions all having noticeable effect on distribution of water content in the boundary layer.

As a reference case we use grid size of $256 \times 256 \times 140$ cells, similar to the one proposed in the intercomparison project, but with uniform grid steps in each direction, i.e., $\Delta x = \Delta y = 100$ m and $\Delta z = 50$ m. Contrary to the COMBLE setup specification, no grid refinement towards the surface is used, and this way we exclude any influence of non-uniform grid steps on the LES filtering. Starting from the reference case we successively coarsen the resolution and study how the LES model reproduces the horizontally averaged and domain-averaged quantities. The horizontal grid step is increased up to $\Delta x = \Delta y = 800$ m, while the vertical grid step is increased up to $\Delta z = 400$ m, i.e., eight-fold compared to the reference computational grid.

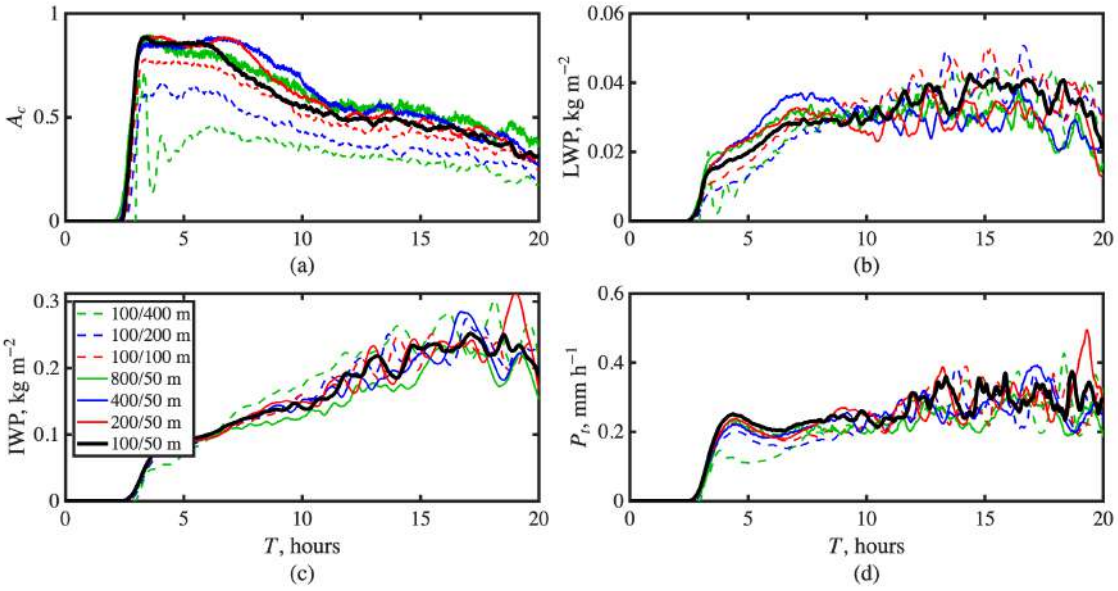

Figure 1. Domain-averaged cloud characteristics: (a) cloud area fraction A_c, (b) liquid water path, (c) ice water path and (d) total precipitation P_t with the decrease in horizontal (solid lines) and vertical (dashed lines) resolution of the large-eddy simulation model. The bold black line denotes the reference simulations on the finest computational grid

Figure 1 shows the domain-averaged characteristics of the key cloud properties: the cloud area fraction (Fig. 1a) A_c, the distribution of total water content (Fig. 1b and Fig. 1c) and the total precipitation rate P_t (Fig. 1d), which is related to ice-phase sedimentation, with negligible contribution from the liquid-phase. The total water content is given in terms of horizontally-averaged values of liquid water path (LWP) and ice water path (IWP):

$$\mathrm{LWP}(x,y) = \int_0^{L_z} \rho_0 q_{\mathrm{liquid}} dz \equiv \int_0^{L_z} \rho_0 \left(q_{\mathrm{c}} + q_{\mathrm{r}}\right) dz,$$
$$\mathrm{IWP}(x,y) = \int_0^{L_z} \rho_0 q_{\mathrm{solid}} dz \equiv \int_0^{L_z} \rho_0 \left(q_{\mathrm{i}} + q_{\mathrm{s}} + q_{\mathrm{g}}\right) dz.$$

Here and hereafter we drop the LES-filtering notation, i.e., $\overline{(\cdot)}$, when denoting the model fields to make the presentation of results more concise.

The decrease in vertical resolution (dashed lines in Fig. 1) has the most effect on cloudy boundary layer characteristics. In particular, it significantly reduces the cloud area fraction,

damps the liquid-phase and, to a lesser extent, the ice-phase water content. This in turn affects the precipitation intensity at the early stages of cold-air outbreak, which is mostly due to ice and snow hydrometeors. At the later stages (after 10 hours from the start of simulations, when the cloud top reaches around 2000 m) the boundary layer is sufficiently resolved even with the coarsest grid step of 400 m, and the water content and precipitation estimates almost match the reference case. Notably, the increase of grid steps (solid lines in Fig. 1) in the horizontal directions has a minor influence even on A_c and any other domain-averaged quantities, with only notable excessive condensation during the initial growth of convective boundary layer.

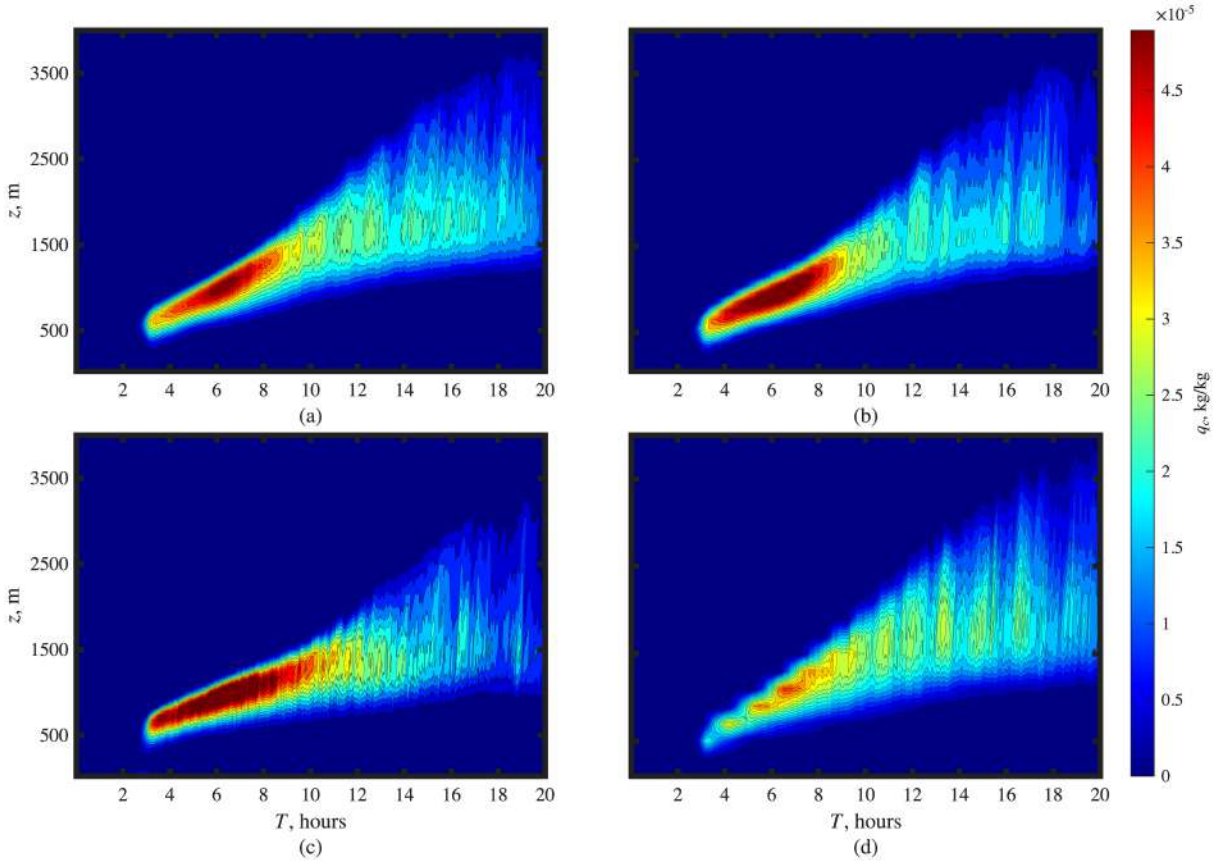

Figure 2. Horizontally-averaged cloud droplet water content, q_c, depending on the grid resolution: (a) reference case with $\Delta_x = \Delta_y = 100$ m, $\Delta z = 50$ m, (b) two-fold decrease in horizontal and vertical resolution, (c) coarsening in horizontal direction to $\Delta x = \Delta y = 800$ m, (d) coarsening in vertical direction to $\Delta z = 200$ m

The horizontally averaged cloud droplet (q_c), ice (q_i) and snow combined with graupel ($q_s + q_g$) water content depending on the resolution of the LES model are shown in Figs. 2, 3 and 4, respectively. The two-fold increase of grid steps in both horizontal and vertical resolution, see Figs. 2–4b, only slightly influences the results. Approaching the coarsest resolution in horizontal directions, $\Delta x = \Delta y = 800$ m (Figs. 2–4c), shows that even though the convective boundary layer growth rate is reduced, resulting in more pronounced saturation and formation of cloud droplets, the ice formation mechanisms and the overall ice-phase water content remains only slightly affected, including the distribution with height of precipitating snow and graupel. When the vertical grid step approaches 200 m (Figs. 2–4d) the entrainment layer at the initial stages is under-resolved suppressing the formation of liquid-phase cloud. This also results in

a more thicker distribution of ice water content, in part suppressing conversion to snow and precipitation before and during the transition from stratocumulus to cumulus.

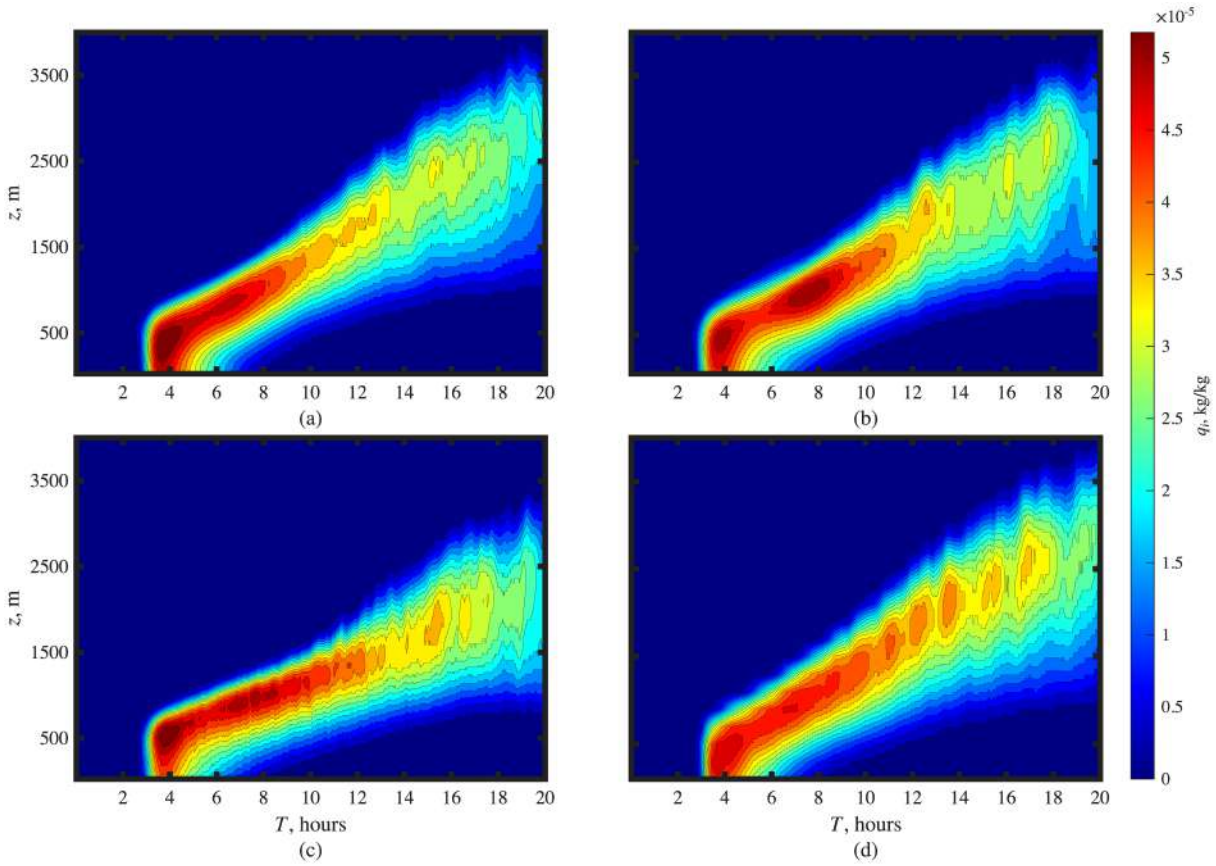

Figure 3. Horizontally-averaged ice water content, q_i, depending on the grid resolution as given in Fig. 2

Our findings show that the developed LES model is capable to reproduce the CAO case characteristics even with highly coarse horizontal resolution of 800 m, while the maximum CBL depth is around 3 km. The horizontal grid resolution only slightly affects the distribution of water content if the turbulence dynamics and the structure of CBL are even barely reproduced. This shows good promise in using the LES model with the dynamic closure approach, applied to momentum, and both heat and moisture transport, to study complex mixed-phase cloud dynamics. On the other hand, as the cloud formation processes are strongly tied with entrainment/detrainment of air, the vertical resolution appears to be more important. While the grid step of 400 m in the vertical direction appears too coarse and unable to resolve the initial growth of boundary layer, the modeling results during the stratocumulus to cumulus transition appear sensitive to even finer resolutions up to 100 m in domain-averaged and horizontally-averaged characteristics, implying also the sensitivity to subgrid closure.

4.3. Computational Performance

To assess the computational performance of the LES model with embedded two-moment bulk microphysics scheme on GPUs, we consider two distinct numerical setups proposed in the COMBLE intercomparison project [23]: the *liquid-only* setup, where only processes related with cloud and rain droplets occur and any ice formation or transport of ice water content is excluded,

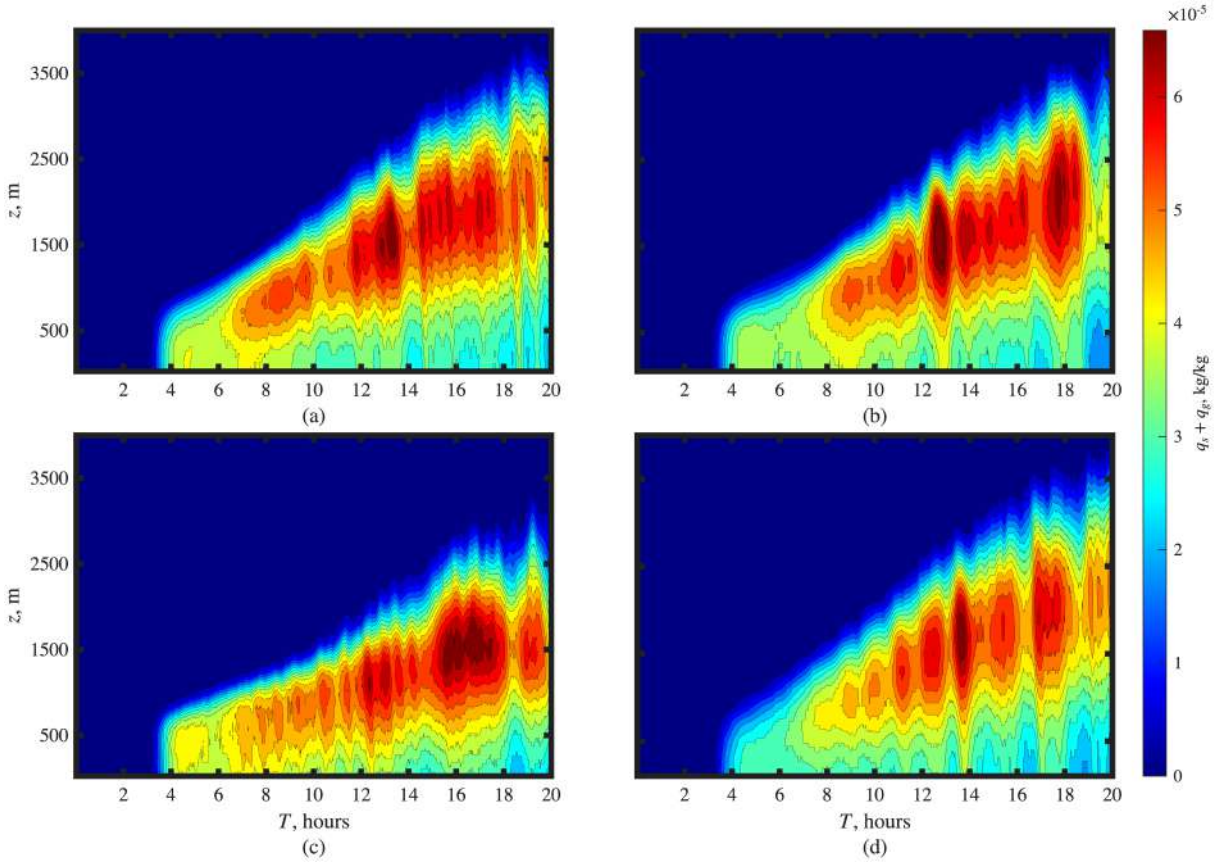

Figure 4. Horizontally-averaged snow and graupel water content, $q_s + q_g$, depending on the grid resolution as given in Fig. 2

and the *mixed-phase* setup with all the liquid- and solid-phase hydrometeors. For the *liquid-only* microphysics we use the saturation adjustment procedure, i.e., the q_c is diagnostic, while the number concentration of cloud droplets, N_c, is fixed. All numerical tests were performed on the Lomonosov-2 supercomputer on nodes with an Intel Xeon Gold 6142 CPUs and NVIDIA V100 GPUs.

To verify the implementation on GPU of the cloud microphysics scheme, the simulations of COMBLE scenario were compared with those obtained on central processing units. Turbulent convective cloud systems are highly nonlinear and we do not expect that the trajectories in both runs would match each other even with minor implementation differences, e.g. order of finite-precision arithmetic operations. The computational grid in these simulations was $128 \times 128 \times 75$ cells, which corresponds to horizontal resolution $\Delta x = \Delta y = 200$ m and a vertical grid step of around $\Delta z \sim 90$ m. Figure 5 shows the difference between the averaged in horizontal directions vertical profiles of ice and snow water content in CPU and GPU runs for the *mixed-phase* case. While the observed differences appear substantial in the later half of simulations, where strong precipitation events occur, we stress that they are within the ensemble spread of LES model for this CAO case. This is also evident in comparison of CPU-GPU implementation results for domain-averaged quantities – liquid and ice water paths shown in Fig. 6, where the relative differences are much smaller.

The two-moment cloud microphysics scheme accounts for circa 50% of total computational time on single CPU core. This is the most computationally demanding part of model time-

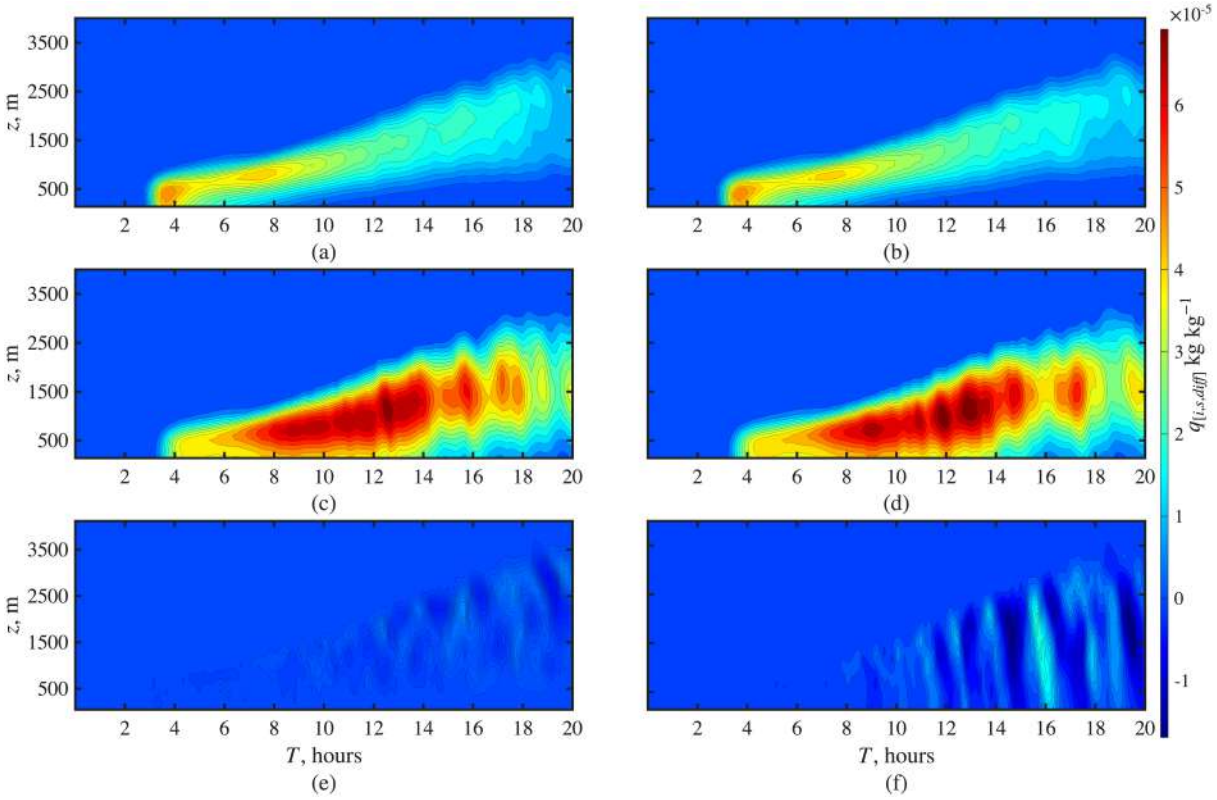

Figure 5. Time evolution of horizontally-averaged vertical profiles for ice, q_i, (a, b) and snow, q_s, (c, d) water content and their respective differences (e, f) between CPU- (a, c) and GPU-based (b, d) implementations in *mixed-phase* case

step, projection method used for solving equations (1) and (2) takes the second place and the dynamic LES closure occupies the third place. This warrants the next part of our study – investigating to what extent the porting of cloud microphysics to GPU architecture could improve the computational performance of the large-eddy simulation model of cloudy boundary layers.

To facilitate these tests, we performed a set of numerical experiments with two-moment cloud microphysics scheme for a range of grid sizes: from $128 \times 128 \times 75$ up to $512 \times 512 \times 75$ cells. Note that for *mixed-phase* case the largest grid size is slightly lower ($576 \times 256 \times 75$ cells) because of increased memory demand – storing additional solid-phase hydrometeor fields and their tendencies makes model reach the 16 GB VRAM limit of V100 devices.

The speedup estimates of running the LES model on GPUs as compared with CPU-only implementation are given in Figs. 7 and 8 for *liquid-only* and *mixed-phase* simulations, respectively. Figure 7 shows the speedup of the entire model (Fig. 7a) and its individual components (Fig. 7b, c and d) for the *liquid-only* case, comparing performance of single GPU with single CPU core. With the increase in grid size (N) the speedup increases for the surface layer flux scheme (Fig. 7b: surface layer), the projection method for solving the momentum equations with incompressibility constraint (Fig. 7c: momentum eq.), and, in particular, the implementation of the BiCGstab algorithm with multigrid preconditioner for solving the finite-difference Poisson equation (Fig. 7c: poisson eq.). The opposite behavior is observed for other components (Fig. 7b, c, d), including the cloud microphysics scheme. This dependence of GPU performance on grid resolution is evident for the *mixed-phase* simulations as well (Fig. 8). In both cases the microphysics scheme (Fig. 7b and Fig. 8b), while being one of the most time-consuming,

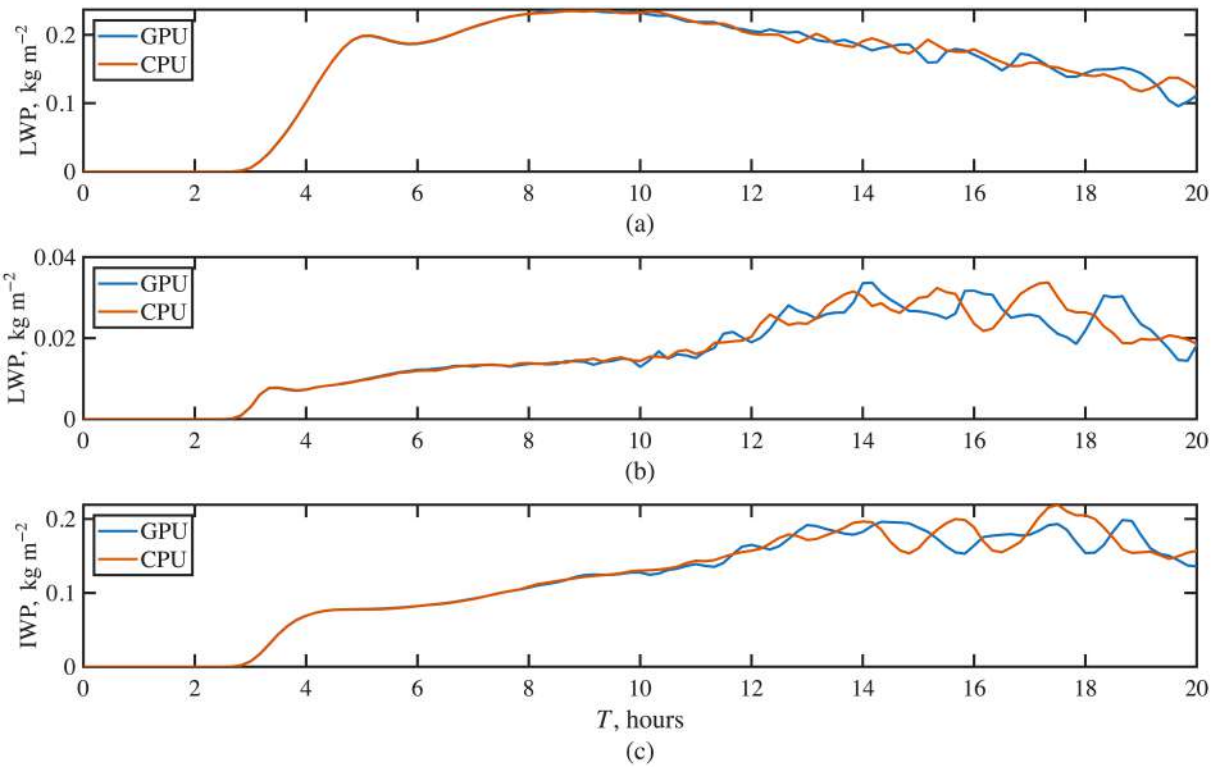

Figure 6. Differences between CPU- and GPU-based implementation of the LES model for liquid water path (LWP) in (a) *liquid-only* and (b) *mixed-phase* cases, (c) ice water path (IWP)

achieves the most significant reduction in run-time over CPU implementation with the speedup in *mixed-phase* well over 200 times compared to single CPU core. Notably, the overall model performance is hindered by less efficient GPU-implementation of explicit in time numerical methods for solving advection-diffusion type equations for liquid/solid water potential temperature Θ, total water content q, mixing ratios q_a and number concentrations N_a of all the hydrometeors, where $a = [c, r, i, s, g]$. Optimization of tracer transport algorithms (see analysis in [12]) seems especially relevant for the *mixed-phase* simulations, as the two-moment microphysics scheme may involve solving ten additional transport equations.

Next, we focus on MPI-scalability of the LES model, shown in Figs. 9 and 10. This evaluation is important for both CPU- and GPU-based implementations. For the former, efficient MPI-scaling is crucial to shorten single GPU-card-to-core gap, and, for the latter, memory constraints on the GPU (compared to CPU) require the use of multiples of devices for very large grids. In numerical tests we enlarged the computational domain in each horizontal direction up to 100 km, resulting in a grid comprising $512 \times 512 \times 75$ cells.

The LES model (Fig. 9a) and almost all of its components (Fig. 9b, c, d, e, f) exhibit a near-linear speedup with increase in the number of MPI processes for CPU-based implementation. The only notable exceptions are the microphysics scheme (Fig. 9b: microphysics) and computations related to evaluation of virtual potential temperature (Fig. 9c: state eq.). This could be attributed to additional MPI communications performed in these parts of the model.

For the MPI-CUDA hybrid implementation we bind each GPU to a separate MPI process, while the speedup is calculated relative to the run time achieved on 2 MPI processes due to insufficient memory available on a single GPU. The results for the GPU-based implementation (Fig. 10) show that MPI-scaling is less efficient, compared with baseline CPU results. In par-

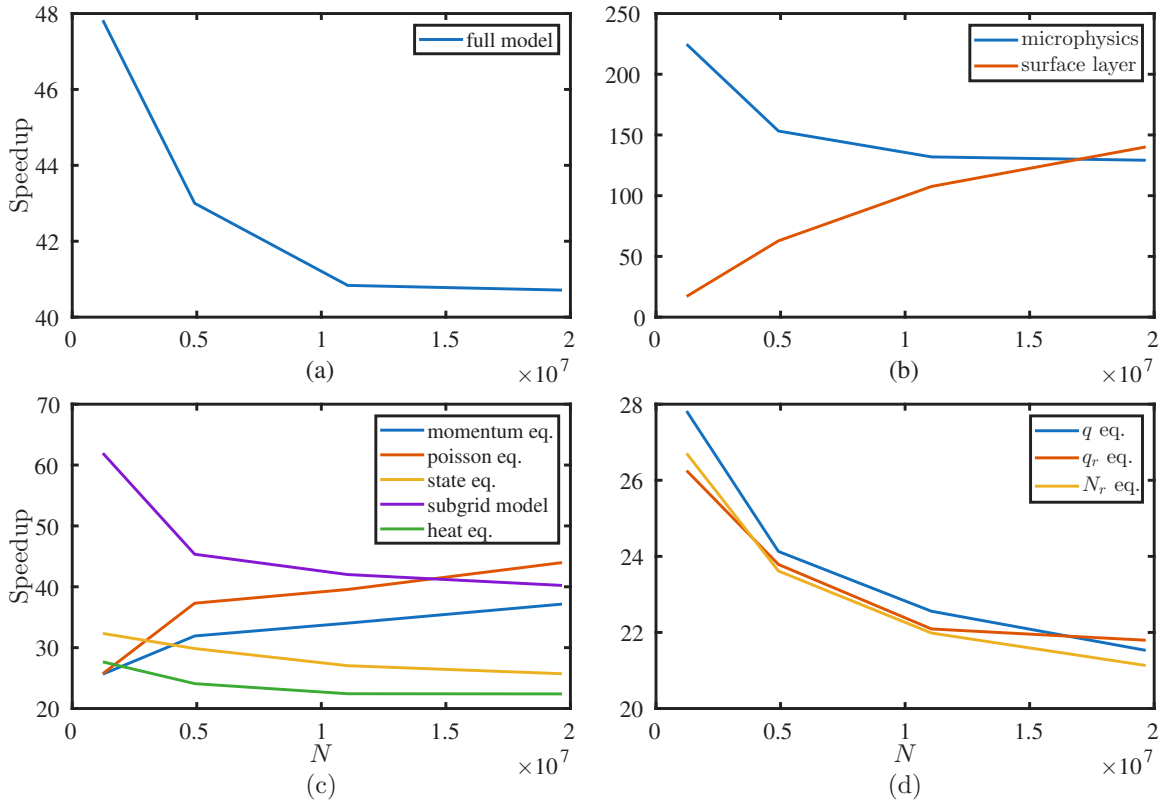

Figure 7. Single GPU over single CPU core implementation speedup of the LES model and its components for *liquid-only* simulations depending on the number of grid cells N

ticular, additional communications with CPU-GPU data transfers thwart the scalability of the dynamics part of the model (Fig. 10c: momentum eq. and poisson eq.). This is primary related to communications and grid coarsening applied in the multigrid method (Fig. 10c: poisson eq.). The reason for poor MPI scalability for the surface flux layer calculations (Fig. 10b: surface layer) appears to be rather small workload, since those calculations are performed only with 2D surface layer data. On the other hand, almost 4-times speedup of the model on 16 GPUs (compared with run time on 2 GPUs) is due to highly-efficient MPI-scaling of the transport equations and, especially, the microphysics scheme.

Some further improvements on MPI-scaling could be expected on novel NVIDIA GPU devices interconnected via high-bandwidth communication links called NVLink. This allows for effective memory exchange between GPUs without utilising CPU RAM (Random Access Memory). For instance, NVLink connection between two A100 GPUs provides 600 GB/s bidirectional bandwidth. Moreover, peer-to-peer exchange between the GPUs on the different computational nodes can be performed if they are connected using RDMA (Remote Direct Memory Access) supported communication links: Infiniband or RoCE – RDMA over Converged Ethernet. Such CPU-excluding data transfers can be implemented in LES models with the communication libraries introduced by coprocessor suppliers (e.g., NVIDIA or AMD). Particularly, NCCL (NVIDIA Collective Communications Library) provides optimized multi-GPU and multi-node communication primitives.

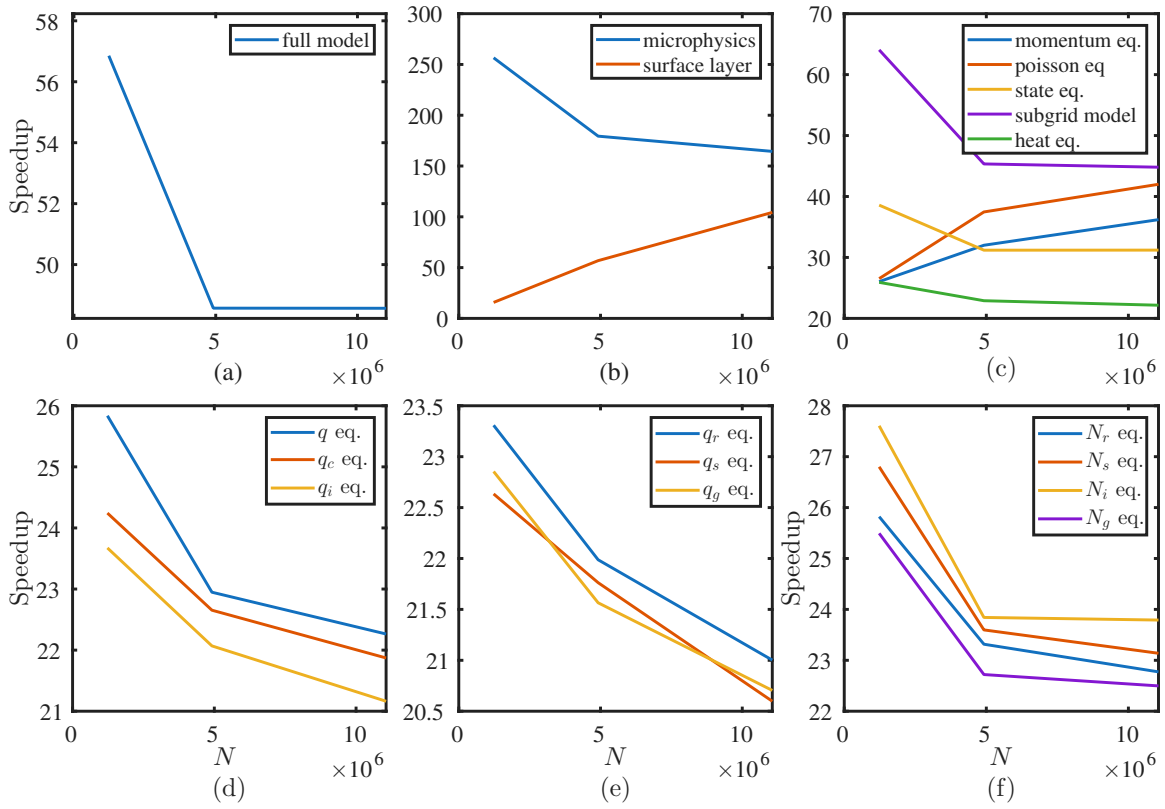

Figure 8. Single GPU over single CPU core implementation speedup of the LES model and its components for *mixed-phase* simulations depending on the number of grid cells N

Conclusions

In this paper we discussed the development of the large-eddy simulation model supplemented with two-moment bulk cloud microphysics scheme for GPU-based HPC systems. The model is based on the dynamic approach for calculation of subgrid scale fluxes, applied to both heat and moisture transport. The analysis of large-eddy simulation of an intense cold-air outbreak case in the Arctic showed little sensitivity in reproducing bulk characteristics of mixed-phase cloudy convection to horizontal grid resolution. On the other hand, the results highlight stronger dependence on vertical resolution even in cases where the CBL dynamics could be expected to be well-resolved by the LES model. Here the grid coarsening led to pronounced reduction in cloud cover, weakened cloud formation during the stratocumuls to cumulus transition, but overall only slightly affected domain-averaged water content and precipitation estimates. In this regard future studies of cloud transition mechanisms during CAO should take into account the possible significant sensitivity to vertical grid resolution and subgrid closure in the LES approach.

The performance evaluation tests demonstrated that GPU implementation provides up to 200 times higher computing performance than single CPU core (or more than 10 times per a CPU node) for computationally demanding cloud microphysics schemes. Numerical solution of tracer transport equations represents one of the main bottlenecks in GPU implementation, relative to other components of the model, achieving a performance comparable to only 1.5 CPU nodes. With the overall estimated threefold speedup of the LES model on graphics processing unit compared to CPU node, adopting code to GPU allows to expand possible range of domain

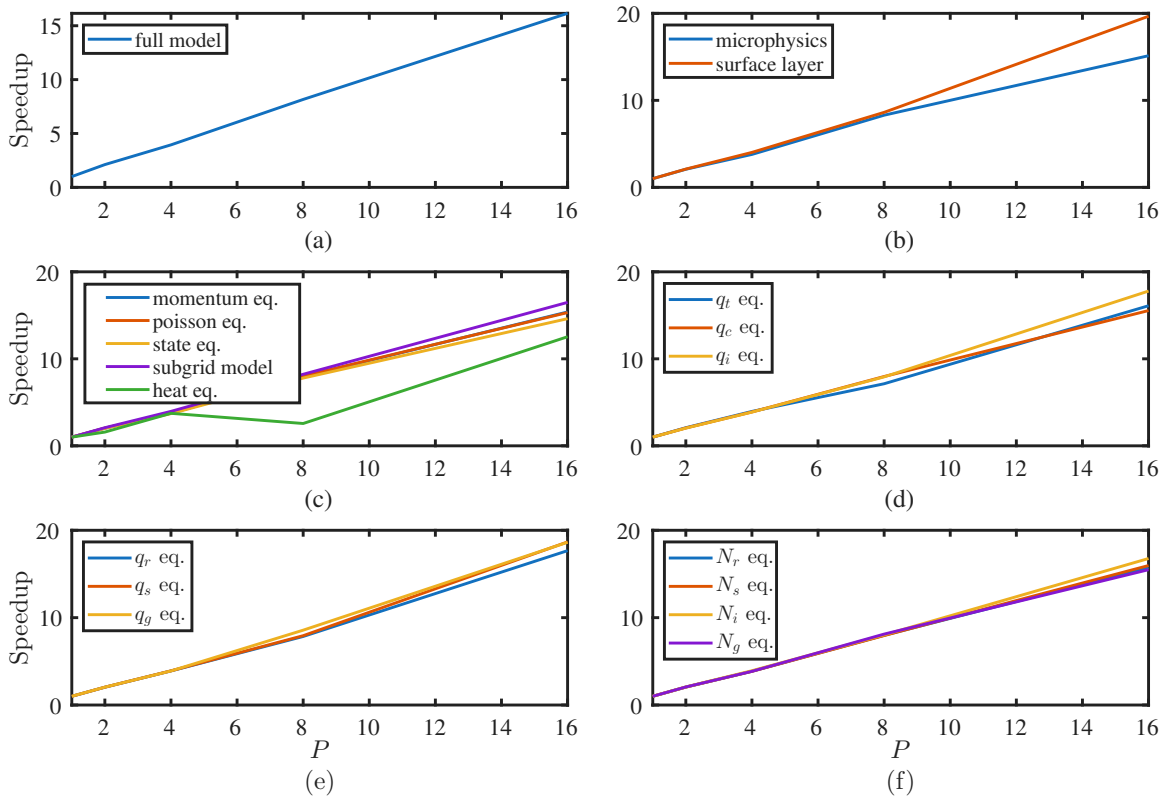

Figure 9. MPI-scalability of the CPU-based implementation of the LES model and its components, P is the number of MPI processes

and grid sizes. This is a prerequisite for studies of complex mixed-phase cloud processes and cloud organizations.

One of the main concerns is related to inefficient MPI multi-GPU scaling of the LES model, which requires further improvement. While the cloud microphysics scheme achieves even super-linear speedup when using 16 GPUs, the overall efficiency of the LES model is hampered by the implementation of multigrid method for solving finite-difference approximation of the Poisson equation, which heavily relies on data coarsening to achieve higher convergence rates and involves a significant amount of communications. These findings suggest the necessity for further optimization of MPI data transfers in GPU-based LES models. In this regard, such improvements could be achieved by excluding CPU RAM in MPI communications, using specialized technologies (e.g., NVLink) and libraries (e.g. NCCL) for device-to-device high bandwidth link between state-of-the-art GPUs.

Acknowledgements

The research is carried out using the equipment of shared research facilities of HPC computing resources at Lomonosov Moscow State University. This study was supported by the Russian Science Foundation (project 25-77-20011; development of the LES model and adoption to multi-GPU computations) and by the Ministry of Education and Science of the Russian Federation (the program of the Moscow Center of Fundamental and Applied Mathematics under agreement No. 075-15-2025-345; implementation evaluation and performance experiments analysis).

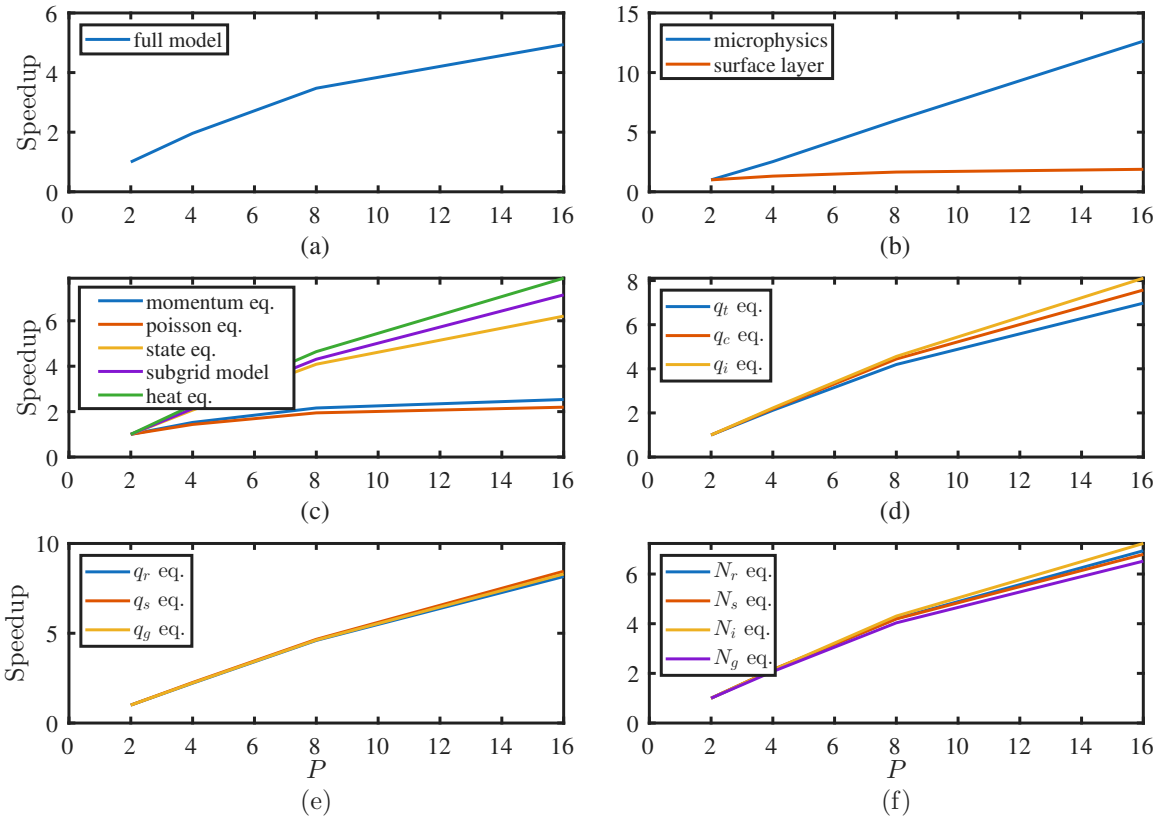

Figure 10. MPI-scalability of the GPU-based implementation of the LES model and its components, P is the number of MPI processes

References

1. Baldauf, M., Seifert, A., Förstner, J., *et al.*: Operational convective-scale numerical weather prediction with the cosmo model: Description and sensitivities. Monthly Weather Review 139, 3887–3905 (12 2011). https://doi.org/10.1175/MWR-D-10-05013.1

2. Bhattacharjee, S., Mortikov, E., Debolskiy, A., *et al.*: Direct numerical simulation of a turbulent channel flow with Forchheimer drag. Boundary-Layer Meteorology 185(2), 259–276 (2022). https://doi.org/10.1007/s10546-022-00731-8

3. Bieringer, P.E., Piña, A.J., Lorenzetti, D.M., *et al.*: A Graphics Processing Unit (GPU) Approach to Large Eddy Simulation (LES) for Transport and Contaminant Dispersion. Atmosphere 12(7), 890 (2021). https://doi.org/10.3390/atmos12070890

4. Bigg, E.K.: The formation of atmospheric ice crystals by the freezing of droplets. Quarterly Journal of the Royal Meteorological Society 79(342), 510–519 (1953). https://doi.org/10.1002/qj.49707934207

5. Bou-Zeid, E., Meneveau, C., Parlange, M.: A scale-dependent Lagrangian dynamic model for large eddy simulation of complex turbulent flows. Physics of Fluids 17(2), 025105 (2005). https://doi.org/10.1063/1.1839152

6. Brown, D.L., Cortez, R., Minion, M.L.: Accurate projection methods for the incompressible Navier–Stokes equations. Journal of Computational Physics 168(2), 464–499 (2001). https://doi.org/10.1006/jcph.2001.6715

7. Cotton, R.J., Field, P.R.: Ice nucleation characteristics of an isolated wave cloud. Quarterly Journal of the Royal Meteorological Society 128(585), 2417–2437 (2002). https://doi.org/10.1256/qj.01.150

8. Debolskiy, A.V., Mortikov, E.M., Poliukhov, A.A.: Computational efficiency and adaptation of radiation transfer module within Large-eddy simulation model. Numerical Methods and Programming 26(4), 515–533 (2025). https://doi.org/10.26089/NumMet.v26r434

9. Debolskiy, A.V., Mortikov, E.V., Glazunov, A.V., Lüpkes, C.: Evaluation of surface layer stability functions and their extension to first order turbulent closures for weakly and strongly stratified stable boundary layer. Boundary-Layer Meteorology 187(1), 73–93 (2023). https://doi.org/10.1007/s10546-023-00784-3

10. Ding, C., He, Y.: A ghost cell expansion method for reducing communications in solving PDE problems. In: Proceedings of the 2001 ACM/IEEE Conference on Supercomputing. p. 50. SC '01, Association for Computing Machinery, New York, NY, USA (2001). https://doi.org/10.1145/582034.582084

11. Donahue, A., Caldwell, P.: Impact of physics parameterization ordering in a global atmosphere model. Journal of Advances in Modeling Earth Systems 10(2), 481–499 (2018). https://doi.org/10.1002/2017MS001067

12. Gaschuk, E.M., Ezhkova, A.A., Onoprienko, V.A., *et al.*: Passive tracer transport in ocean modeling: implementation on GPUs, efficiency and optimizations. Lobachevskii Journal of Mathematics 44(8), 3040–3058 (2023). https://doi.org/10.1134/S1995080223080152

13. Geerts, B., Giangrande, S., Mcfarquhar, G., *et al.*: "COMBLE" Beginnings: The Cold-Air Outbreaks in the Marine Boundary Layer Experiment. Bulletin of the American Meteorological Society 104, 327–330 (03 2025). https://doi.org/10.1175/BAMS-D-21-0044.A

14. Geerts, B., Giangrande, S.E., McFarquhar, G.M., *et al.*: The COMBLE Campaign: A study of marine boundary layer clouds in Arctic cold-air outbreaks. Bulletin of the American Meteorological Society 103(5), E1371–E1389 (2022). https://doi.org/10.1175/BAMS-D-21-0044.1

15. Germano, M., Piomelli, U., Moin, P., Cabot, W.H.: A dynamic subgrid-scale eddy viscosity model. Physics of Fluids A: Fluid Dynamics 3(7), 1760–1765 (1991). https://doi.org/10.1063/1.857955

16. Giorgetta, M.A., Brokopf, R., Crueger, T., *et al.*: ICON-A, the Atmosphere Component of the ICON Earth System Model: I. Model Description. Journal of Advances in Modeling Earth Systems 10(7), 1613–1637 (2018). https://doi.org/10.1029/2017MS001242

17. Gladskikh, D., Ostrovsky, L., Troitskaya, Y., *et al.*: Turbulent transport in a stratified shear flow. Journal of Marine Science and Engineering 11(1), 136 (2023). https://doi.org/10.3390/jmse11010136

18. Glazunov, A., Mortikov, E., Debolskiy, A., Pashkin, A.: Large eddy simulation in the urban environment with simplified and realistic surface morphology. Russian Meteorology and Hydrology 50, 491–506 (2025). https://doi.org/10.3103/S1068373925060056

19. Glazunov, A., Rannik, U., Stepanenko, V., *et al.*: Large-eddy simulation and stochastic modeling of Lagrangian particles for footprint determination in the stable boundary layer. Geoscientific Model Development 9(9), 2925–2949 (2016). https://doi.org/10.5194/gmd-9-2925-2016

20. Glazunov, A.V., Mortikov, E.V., Barskov, K.V., *et al.*: Layered structure of stably stratified turbulent shear flows. Izvestiya, Atmospheric and Oceanic Physics 55(4), 312–323 (2019). https://doi.org/10.1134/S0001433819040042

21. Heus, T., van Heerwaarden, C.C., Jonker, H.J.J., *et al.*: Formulation of the Dutch Atmospheric Large-Eddy Simulation (DALES) and overview of its applications. Geoscientific Model Development 3(2), 415–444 (2010). https://doi.org/10.5194/gmd-3-415-2010

22. Juliano, T., Tornow, F., Fridlind, A.: COMBLE Model-Observation Intercomparison Project Cookbook. https://arm-development.github.io/comble-mip/README.html (2023), accessed: 2025-11-04

23. Juliano, T.W., Tornow, Florian Fridlind, A.M., Ackerman, A.S., *et al.*: The Cold-Air Outbreaks in the Marine Boundary Layer Experiment model-observation intercomparison project (COMBLE-MIP), Part I: Model specification, observational constraints, and preliminary findings. Geoscientific Model Development (2025), (in review)

24. Kadantsev, E., Mortikov, E., Glazunov, A., *et al.*: On dissipation timescales of the basic second-order moments: the effect on the energy and flux budget (EFB) turbulence closure for stably stratified turbulence. Nonlinear Processes in Geophysics 31(3), 395–408 (2024). https://doi.org/10.5194/npg-31-395-2024

25. Kadantsev, E., Mortikov, E., Zilitinkevich, S.: The resistance law for stably stratified atmospheric planetary boundary layers. Quarterly Journal of the Royal Meteorological Society 147(737), 2233–2243 (2021). https://doi.org/10.1002/qj.4019

26. Khain, A.P., Beheng, K.D., Heymsfield, A., *et al.*: Representation of microphysical processes in cloud-resolving models: Spectral (bin) microphysics versus bulk parameterization. Reviews of Geophysics 53(2), 247–322 (2015). https://doi.org/10.1002/2014RG000468

27. Lilly, D.K.: A proposed modification of the Germano subgrid-scale closure method. Physics of Fluids A 4(3), 633–635 (1992). https://doi.org/10.1063/1.858280

28. Lund, T.S.: On the use of discrete filters for large eddy simulation. In: Annual Research Briefs, pp. 83–95. Center for Turbulence Research, Stanford University: Stanford (1997)

29. Maronga, B., Banzhaf, S., Burmeister, C., *et al.*: Overview of the PALM model system 6.0. Geoscientific Model Development 13(3), 1335–1372 (2020). https://doi.org/10.5194/gmd-13-1335-2020

30. Meneveau, C., Lund, T.S., Cabot, W.H.: A Lagrangian dynamic subgrid-scale model of turbulence. Journal of Fluid Mechanics 319, 353–385 (1996). https://doi.org/10.1017/S0022112096007379

31. Morinishi, Y., Lund, T., Vasilyev, O., Moin, P.: Fully conservative higher order finite difference schemes for incompressible flow. Journal of Computational Physics 143(1), 90–124 (1998). https://doi.org/10.1006/jcph.1998.5962

32. Mortikov, E.V.: Numerical simulation of the motion of an ice keel in a stratified flow. Izvestiya, Atmospheric and Oceanic Physics 52(1), 108–115 (2016), https://journal-vniispk.ru/0001-4338/article/view/148416

33. Mortikov, E.V., Debolskiy, A.V.: Direct numerical simulation of stratified turbulent flows and passive tracer transport on HPC systems: Comparison of CPU architectures. Supercomputing Frontiers and Innovations 8(4), 50–68 (2021). https://doi.org/10.14529/jsfi210405

34. Mortikov, E.V., Debolskiy, A.V., Glazunov, A.V., *et al.*: Planetary boundary layer scheme in the INMCM Earth system model. Russian Journal of Numerical Analysis and Mathematical Modelling 39(6), 343–352 (2024). https://doi.org/10.1515/rnam-2024-0029

35. Mortikov, E.V., Glazunov, A.V., Lykosov, V.N.: Numerical study of plane Couette flow: turbulence statistics and the structure of pressure-strain correlations. Russian Journal of Numerical Analysis and Mathematical Modelling 34(2), 119–132 (2019). https://doi.org/10.1515/rnam-2019-0010

36. Ovchinnikov, M., Ackerman, A.S., Avramov, A., *et al.*: Intercomparison of large-eddy simulations of Arctic mixed-phase clouds: Importance of ice size distribution assumptions. Journal of Advances in Modeling Earth Systems 6(1), 223–248 (2014). https://doi.org/10.1002/2013MS000282

37. Reisner, J., Rasmussen, R.M., Bruintjes, R.T.: Explicit forecasting of supercooled liquid water in winter storms using the MM5 mesoscale model. Quarterly Journal of the Royal Meteorological Society 124(548), 1071–1107 (1998). https://doi.org/10.1002/qj.49712454804

38. Sagaut, P.: Large eddy simulation for incompressible flows. Springer (2006). https://doi.org/10.1007/b137536

39. Satoh, M., Stevens, B., Judt, F., *et al.*: Global cloud-resolving models. Current Climate Change Reports 5, 172–184 (2019). https://doi.org/10.1007/s40641-019-00131-0

40. Schalkwijk, J., Jonker, H., Siebesma, A.P., Meijgaard, E.: Weather Forecasting Using GPU-Based Large-Eddy Simulations. Bulletin of the American Meteorological Society 96, 715–723 (2015). https://doi.org/10.1175/BAMS-D-14-00114.1

41. Seifert, A., Beheng, K.D.: A two-moment cloud microphysics parameterization for mixed-phase clouds. Part 2: Maritime vs. continental deep convective storms. Meteorology and Atmospheric Physics 92(1-2), 67–82 (2006). https://doi.org/10.1007/s00703-005-0113-3

42. Seifert, A., Heus, T.: Large-eddy simulation of organized precipitating trade wind cumulus clouds. Atmospheric Chemistry and Physics 13(11), 5631–5645 (2013). https://doi.org/10.5194/acp-13-5631-2013

43. Seifert, A., Beheng, K.D.: A double-moment parameterization for simulating autoconversion, accretion and selfcollection. Atmospheric Research 59-60, 265–281 (2001). https://doi.org/10.1016/S0169-8095(01)00126-0

44. Seifert, A., Stevens, B.: Microphysical scaling relations in a kinematic model of isolated shallow cumulus clouds. Journal of the Atmospheric Sciences 67, 1575–1590 (2010). https://doi.org/10.1175/2009JAS3319.1

45. Siebesma, A.P., Bretherton, C., Brown, A., *et al.*: A large eddy simulation intercomparison study of shallow cumulus convection. Journal of the Atmospheric Sciences 60, 1201–1219 (2003). https://doi.org/10.1175/1520-0469(2003)60<1201:ALESIS>2.0.CO;2

46. Smagorinsky, J.: Global atmospheric modeling and the numerical simulation of climate. In: Hess, W.N. (ed.) Weather and climate modification, pp. 633–686. John Wiley & Sons, Ltd: New York (1974)

47. Suiazova, V., Debolskiy, A., Mortikov, E.: Study of surface layer characteristics in the presence of suspended snow particles using observational data and Large-Eddy Simulation. Izv. Atmos. Ocean. Phys. 60(2), 183–195 (2024). https://doi.org/10.1134/S000143382470021X

48. Suiazova, V., Debolskiy, A., Mortikov, E.: Modeling turbulent flows over a heterogeneous surface using mesoscale and large eddy simulations. Russian Meteorology and Hydrology 50, 417–426 (2025). https://doi.org/10.3103/S106837392505005X

49. Tarasova, M., Debolskiy, A., Mortikov, E., *et al.*: On the parameterization of the mean wind profile for urban canopy models. Lobachevskii Journal of Mathematics 45, 3198–3210 (2024). https://doi.org/10.1134/S1995080224603801

50. Tkachenko, E., Debolskiy, A., Mortikov, E.: Intercomparison of subgrid scale models in large-eddy simulation of sunset atmospheric boundary layer turbulence: Computational aspects. Lobachevskii Journal of Mathematics 42, 1580–1595 (2021). https://doi.org/10.1134/S1995080221070234

51. Tomita, H.: New microphysical schemes with five and six categories by diagnostic generation of cloud ice. Journal of the Meteorological Society of Japan. Ser. II 86A, 121–142 (2008). https://doi.org/10.2151/jmsj.86A.121

52. vanZanten, M.C., Stevens, B., Nuijens, L., *et al.*: Controls on precipitation and cloudiness in simulations of trade-wind cumulus as observed during RICO. Journal of Advances in Modeling Earth Systems 3(2), M06001 (2011). https://doi.org/10.1029/2011MS000056

53. Varentsov, A.I., Mortikov, E.V., Glazunov, A.V., *et al.*: Large-eddy simulation of aerosol transport over different urban local climate zones. Geography, Environment, Sustainability 18(3), 68–79 (2025). https://doi.org/10.24057/2071-9388-2025-3925

54. Voevodin, V., Debolskiy, A., Mortikov, E.: Facilitating the Process of Performance Analysis of HPC Applications. Lobachevskii Journal of Mathematics 44, 3178–3190 (2023). https://doi.org/10.1134/S1995080223080589

55. Wisner, C., Orville, H.D., Myers, C.: A Numerical Model of a Hail-Bearing Cloud. Journal of the Atmospheric Sciences 29(6), 1160–1181 (1972). https://doi.org/10.1175/1520-0469(1972)029<1160:ANMOAH>2.0.CO;2

56. Wu, P., Ovchinnikov, M., Xiao, H., *et al.*: Effect of ice number concentration on the evolution of boundary layer clouds during Arctic marine cold-air outbreaks. Journal of Geophysical Research: Atmospheres 130(3), e2024JD041282 (2025). https://doi.org/10.1029/2024JD041282

57. Zasko, G.V., Glazunov, A.V., Mortikov, E.V., *et al.*: Optimal Energy Growth in Stably Stratified Turbulent Couette Flow. Boundary-Layer Meteorology 187(1), 395–421 (2023). https://doi.org/10.1007/s10546-022-00744-3

58. Zilitinkevich, S., Druzhinin, O., Glazunov, A., *et al.*: Dissipation rate of turbulent kinetic energy in stably stratified sheared flows. Atmospheric Chemistry and Physics 19(4), 2489–2496 (2019). https://doi.org/10.5194/acp-19-2489-2019